Dynamics of a light beam suffering the influence of a dispersing mechanism with tunable refraction index

Diogo Ricardo da Costa and R. Egydio de Carvalho
Universidade Estadual Paulista (UNESP), Instituto de Geociências e Ciências Exatas (IGCE), 13506-900 Rio Claro-SP, Brazil

(Received 5 March 2018; revised manuscript received 28 May 2018; published 30 August 2018)

The dynamics of a monochromatic light beam is studied inside the oval billiard with an inner scatter circle, which can be interpreted as a cross section of a long optical fiber. The outer oval boundary acts as a perfect reflector for the light beam while the scatter circle encloses a medium with changeable refraction index. The light beam refracts when it enters inside this circle and some drastic changes in the phase space are observed. The increase of the refractive index destroys the center of stability in the phase space leading to a spread of scattered light and the islands of traps for the light propagation become more pulverized. Numerical results are presented and discussed.

DOI: 10.1103/PhysRevE.98.022224

I. INTRODUCTION

The topics spatiotemporal chaos (STC) in optics and chaos in nonlinear optics (CNLO) have been widespread in the literature of optical physics [1–3]. The term STC is originally associated with complex dynamical mechanical systems with many degrees of freedom which show chaotic behavior in both space and time [4–6]. It was adapted to optics since spatiotemporal effects, such as chaos [7,8] and pattern formations [9], can appear in the perpendicular planes of electromagnetic fields [10]. CNLO is frequently associated with nonlinear responses of a given medium due to the application of strong electromagnetic fields which is in general manifested in the third-order susceptibility [11]. The control of optical chaos is also intensively reported to stabilize laser behavior to mask communicating information or to improve the performance of optical switches [12]. Chaotic communication systems based on chaos synchronization between emitter and receiver have been present in theoretical and experimental works as well [13–16]. Whispering gallery resonators are borrowed from acoustic physics to nonlinear optical applications as reported in [17]. The connection between deterministic chaos with an optical system is introduced through a Hamiltonian approach in [18]. An important class of Hamiltonian systems is constituted by billiards. Billiards generally correspond to models that qualitatively mimic properties, mechanisms, or effects of more complex systems. A nonlinear mapping, describing the dynamics in the annular billiard [19], is adapted to describe the effects of the refraction index in the dynamics of a light beam [20]. Billiards generally correspond to models that qualitatively mimic properties, mechanisms, or effects of more complex systems. In this current work we present the influence of the nonlinear classical dynamics on the propagation of a light beam in the oval billiard with an inner circular scatter [21]. In the next section we present the main aspects of the model, while in Sec. III we present the numerical results concerning the effects of the position of the inner scatter. In Sec. IV we apply the technique conservative generalized bifurcation diagram [22] to go deeper into the light beam dynamics and in Sec. V we present final remarks. Since the literature on such subjects is so vast, we also refer the reader to the papers cited within the list of references.

II. ABOUT THE MODEL

The oval billiard consists of a circular boundary with unitary radius for the case considered unperturbed. However, this radius is tunable through the expression

$$R(\theta) = 1 + \epsilon \cos(p\theta), \tag{1}$$

where θ is the angular position measured counterclockwise from the horizontal axis. The control parameter $\epsilon > 0$ deforms the circle and p is a positive integer number, which is kept fixed throughout the paper as $p = 2$ to simplify the calculations. The inner scatter circle is built with a radius r^* and eccentricity δ^* which changes the horizontal position of this circle. If $\delta^* > 0$, the circle moves to the left. In Cartesian coordinates, the position of the center of the circle is given by $(-\delta, 0)$, while the position of the billiard boundary is described as

$$X(\theta) = R(\theta)\cos(\theta) \quad \text{and} \quad Y(\theta) = R(\theta)\sin(\theta). \tag{2}$$

In Fig. 1 an example for the external boundary is shown with $p = 2$ and $\epsilon = 0.2$. The internal circle has $r^* = 0.4$ and $\delta^* = 0.5$. We consider that the light beam reflects specularly with this boundary and at the collision point we define the first angular position, called θ_0. The corresponding position in Cartesian coordinates, which we will call the starting point, is then given by

$$(X_0, Y_0) = [X(\theta_0), Y(\theta_0)]. \tag{3}$$

Another important angle is $\alpha \in (0, \pi)$, measured counterclockwise from the tangent line at the collision point until the output light beam, where it is assumed the law incidence angle equals reflection angle. As an illustration, in Fig. 1 we consider a light beam at $\theta_0 = 0.5$ and $\alpha_0 = 0.9$. Some important angles are also necessary to be defined, one of them being the angle ϕ which gives the direction of the

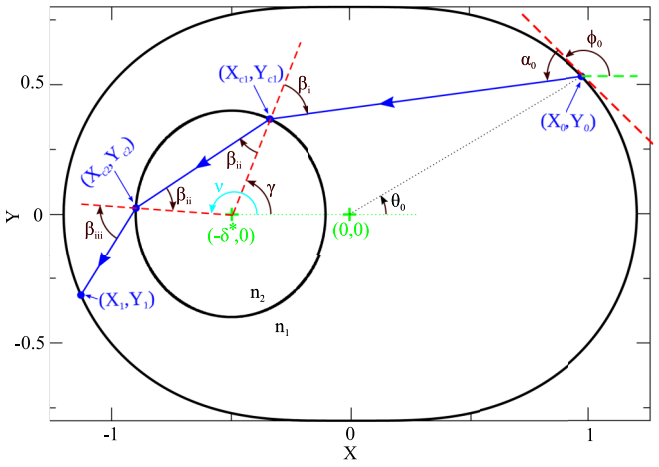

FIG. 1. A light beam starts its motion at (X_0, Y_0). After suffering some refractions with the inner circle, it finally reaches the position (X_1, Y_1). In order to reproduce this figure, consider $p = 2$, $\epsilon = 0.2$, $\delta^* = 0.5$, $r^* = 0.4$, and $\eta = 1.5$. The initial angles were $\theta_0 = 0.5$ and $\alpha_0 = 0.9$.

tangent line at the starting point (X_0, Y_0), and is measured counterclockwise from the horizontal axis as presented in Fig. 1. Therefore

$$\mu_0 = \alpha_0 + \phi_0 \tag{4}$$

gives the initial direction of the output light beam and $\phi_0 = \phi(\theta_0)$. The angle ϕ can be calculated by the following expression:

$$\phi(\theta) = \arctan\left[\frac{Y'(\theta)}{X'(\theta)}\right], \tag{5}$$

where the derivatives are given by

$$X'(\theta) = \frac{\partial R(\theta)}{\partial\theta}\cos(\theta) - Y_0, \tag{6}$$

$$Y'(\theta) = \frac{\partial R(\theta)}{\partial\theta}\sin(\theta) + X_0. \tag{7}$$

From Eq. (1), one can find that

$$\frac{\partial R(\theta)}{\partial\theta} = -\epsilon p\,\sin(p\theta). \tag{8}$$

The main idea in this billiard is to find the position in which the light beam touches the external boundary and in such a situation, we consider that one iteration has been done. To do so, first we need to know the conditions in which the light beam reaches the internal circle [20,21]. It occurs for

$$|R(\theta_0)\sin(\theta_0 - \mu_0) - \delta^*\sin(\mu_0)| \leqslant r^*. \tag{9}$$

If this condition is not satisfied, the light beam does not cross the inner circle and we call it condition (i); then it reaches the external boundary directly. On the other hand, we define condition (ii) when this equation is satisfied and therefore the light beam crosses the inner circle.

A. Condition (i): Light beam does not reach the internal circle

Let us start by describing condition (i). A light beam starting at (X_0, Y_0) reaches the external boundary directly at the position $(X_1, Y_1) = [X(\theta_1), Y(\theta_1)]$. The main idea here is to solve the following transcendental equation [21]:

$$F(\theta_1) = Y_0 - Y_1 + \tan(\mu_0)[X_1 - X_0] = 0, \tag{10}$$

in order to get the new collision point (X_1, Y_1). This equation needs to be solved numerically. To do so, one can vary the value of $\theta_1 \in [0, 2\pi)$ and we evaluate the value of $F(\theta_1)$ through Eq. (10). After finding an interval that contains the solution, we use a bisection method until $F(\theta_1) < 10^{-13} \cong 0$. After obtaining the solution θ_1 we find the positions X_1 and Y_1 and next we can find $\phi_1 = \phi(\theta_1)$ using Eq. (5). Therewith, the new angle α_1 can be obtained by

$$\alpha_1 = \phi_1 - \mu_0. \tag{11}$$

Hence, the new angles θ_1 and α_1 were obtained. In such a situation we say that one iteration of the mapping has been done. We restart the light dynamics by considering $\theta_0 = \theta_1$ and $\alpha_0 = \alpha_1$.

B. Condition (ii): Light beam reaching the internal circle

Now let us describe what happens in condition (ii), which occurs when condition (9) is true and then the light beam crosses the internal circle. Hence one can start calculating the angle β_i, as shown in Fig. 1. After some calculations [21] and from geometric considerations, it is possible to show that

$$\beta_i = \arcsin\left[\frac{R(\theta_0)\sin(\theta_0 - \mu_0) - \delta^*\sin(\mu_0)}{r^*}\right]. \tag{12}$$

We define the point (X_{c1}, Y_{c1}) as the position where the light beam touches the inner circle. Drawing the normal of this circle passing through (X_{c1}, Y_{c1}) one can calculate the angle β_i, measured from the normal to the incident ray. In the example shown in Fig. 1 the angle β_i is negative because it was measured clockwise.

Considering the Snell-Descartes law, one can find the refracting angle β_{ii}, which is given by

$$\beta_{ii} = \arcsin\left[\frac{1}{\eta}\sin(\beta_i)\right], \tag{13}$$

where $\eta = \frac{n_2}{n_1}$ is the ratio between the refraction indexes, where n_2 is the refraction index inside the circle and n_1 is the refraction index outside the circle, i.e.. inside the external oval billiard. After entering into the circle, the light beam direction changes and we need the auxiliary angles

$$\mu' = \mu_0 - \beta_i + \beta_{ii} \tag{14}$$

and

$$\gamma = \mu_0 + \pi - \beta_i \mod(2\pi), \tag{15}$$

where γ is measured counterclockwise from the horizontal line to the normal, of the inner circle, at the incident point. The position (X_{c1}, Y_{c1}) in which the light beam enters in the inner circle is calculated through

$$X_{c1} = r^*\cos(\gamma) - \delta^* \quad \text{and} \quad Y_{c1} = r^*\sin(\gamma). \tag{16}$$

However, to obtain X_2 and Y_2 it is necessary to calculate the angle ν (see Fig. 1). After some geometric considerations, one can find that

$$\nu = \gamma + \pi + 2\beta_{ii}, \tag{17}$$

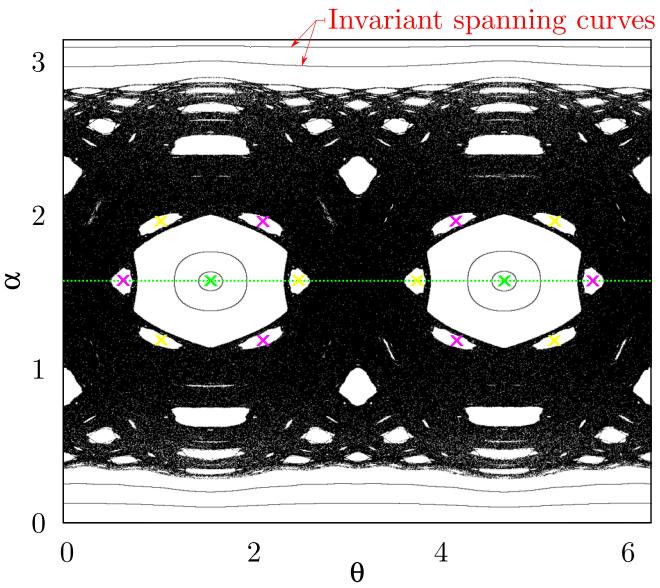

FIG. 2. Phase space α vs θ for the oval billiard with $p = 2$, $\epsilon = 0.1$ and without the internal circle ($r^* = 0$). The green crosses in the center of the huge islands ($\theta = \pi/2$ and $\theta = 3\pi/2$) highlight a period two fixed point.

where γ was calculated using Eq. (15). The coordinates (X_{c2}, Y_{c2}) are calculated by the following expression:

$$X_{c2} = r^* \cos(\nu) - \delta^* \quad \text{and} \quad Y_{c2} = r^* \sin(\nu). \tag{18}$$

The light beam then reaches (X_{c2}, Y_{c2}) and suffers another refraction, where the angle β_{iii} can be calculated using again the Snell-Descartes law. It is easy to see that β_{iii} is equal to β_i. After suffering the refraction, the light beam direction is changed and its angular coefficient is given by

$$\mu'' = \mu_0 + 2\beta_{ii} - 2\beta_i. \tag{19}$$

In order to find the position (X_1, Y_1) in which the light beam attains the external boundary, one needs to consider the following changes of variables:

$$X_0 = X_{c2}, \quad Y_0 = Y_{c2}, \quad \text{and} \quad \mu_0 = \mu''. \tag{20}$$

After that, one needs to solve the transcendental equation (10), where it is possible to find the angle θ_1. The new angle α_1 is calculated using Eq. (11).

Finally, to conclude we update the mapping considering $\theta_0 = \theta_1$ and $\alpha_0 = \alpha_1$. In such case we say that one iteration of the mapping has been done.

III. NUMERICAL RESULTS

First of all, let us start by showing the phase space for the regular oval billiard without the internal circle, which can be done considering $r^* = 0$ and perfect reflection on the boundary. In Fig. 2 a phase space for $\epsilon = 0.1$ and $p = 2$ (classical oval billiard) is shown. As one can see, the phase space contains a huge chaotic sea (black region of the phase space). Some invariant spanning curves are highlighted in the figure limiting the *size* of the chaotic sea. In particular, two huge periodic islands are observed, where in their centers ($\theta = \pi/2$ and $\theta = 3\pi/2$) it is possible to see a period two stable fixed point (marked as the green crosses). Many other periodic islands are observed in such a figure, with different periods.

When we introduce the inner circle in the system (with different refraction index), we change some special portions of the phase space shown in Fig. 2 (of course, when considering the same values of $p = 2$ and $\epsilon = 0.1$). We will focus on the case of $p = 2$ and $\epsilon = 0.1$ because it resumes what are the changes expected when introducing the circle, but other values of p and ϵ can also be studied.

We start by introducing the inner circle in the center of the figure ($\delta^* = 0$), where the radius is $r^* = 0.2$ and $\eta = 1.1$ (remember that $\eta = n_2/n_1$). The result is shown in Fig. 3(a). The red portion of the phase space is important, because it represents situations in which an initial condition θ_0 and α_0 led us to have a collision with the inner circle. On the other hand, if we are outside the red region (black portions of the phase space), it means that an initial condition θ_0 and α_0 does not lead us to reach the inner circle.

Now it is interesting to compare Fig. 3 with Fig. 2. As one can see, the important difference is observed near the two huge periodic islands shown in Fig. 2, which are smaller in Fig. 3(a). We also see many small periodic islands around the two periodic islands. Hence, we only see changes around the red regions of the phase space. The dynamics near $\theta = \pi/2$ and $\theta = 3\pi/2$ is highly influenced by the refractive circle put in the center of the billiard.

In order to see the influence of the position of the circle, we start by increasing the value of δ^* to 0.1926, as shown in Fig. 3(b). Something interesting happens when we consider this value of δ^*. As one can see, the two big periodic islands in the center of Fig. 2 disappear. Other periodic islands near $\theta = \pi/2$ and $\theta = 3\pi/2$ appear and their shape, size, and period have suffered considerable changes. The original fixed points were stable and now they bifurcated to unstable.

Increasing the value of δ^* to 0.2448 makes the periodic islands near $\theta = \pi/2$ and $\theta = 3\pi/2$ start appearing again [see Fig. 3(c)]. Now for $\delta^* = 0.3510$, as shown in Fig. 3(d), one can see that these two periodic islands are much larger. This point becomes clearer in Fig. 3(e) for $\delta^* = 0.6129$. In such a figure there are many island chains surrounding the huge islands.

Now we consider the limit case, where the value of δ^* is maximum. It can be done considering [21]

$$\delta^*_{\max} = 1 + \epsilon - r^*, \tag{21}$$

where for $r^* = 0.2$ and $\epsilon = 0.1$ is given by $\delta^*_{\max} = 0.9$. The result is shown in Fig. 3(f). The red region suffers a great deformation, stretching from $\alpha = 0$ to $\alpha = \pi$, which causes the destruction of all invariant spanning curves (also known as whispering gallery orbits) and the dynamics almost recovered its regular shape and size presented in Fig. 2. As a consequence, the *size* of the chaotic sea increases. So, if one wants to create a bigger region of chaotic sea, start by using the case $\delta^* = \delta^*_{\max}$ through Eq. (21).

IV. CONSERVATIVE GENERALIZED BIFURCATION DIAGRAM

As shown in Refs. [21,22], we can obtain the conservative generalized bifurcation diagram (CGBD) for our system. It

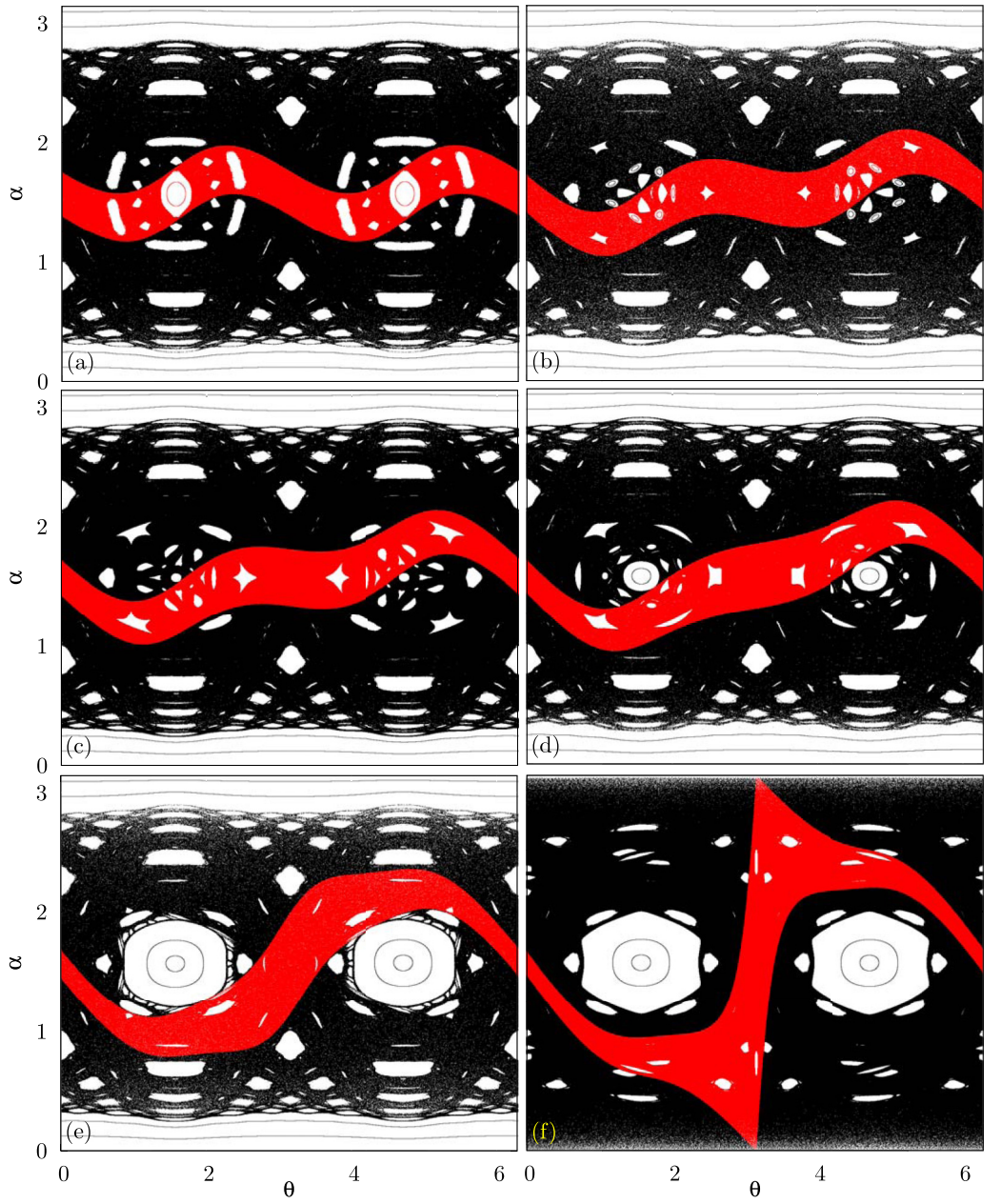

FIG. 3. Phase space for different values of δ^*. (a) $\delta^* = 0$; (b) $\delta^* = 0.1926$; (c) $\delta^* = 0.2448$; (d) $\delta^* = 0.3510$; (e) $\delta^* = 0.6129$; (f) $\delta^* = \delta^*_{\max} = 0.9$. The red color represents values in the phase space in which the light beam suffered a refraction with the inner circle. The other control parameters used were $p = 2$, $\epsilon = 0.1$, $r^* = 0.2$, and $\eta = 1.1$.

is used to show what happens with some fixed points, their stability, and to highlight direct and inverse parabolic bifurcations. To do so, we could first of all study the Lyapunov exponent of the system. Indeed, it is possible, but depending on the system, it is not so easy to obtain. As our model presents too many equations, it is not so easy to find the Jacobian matrix and as consequence, the Lyapunov exponents. So, we decided to use two different observables, which can highlight the bifurcations as well.

To understand how to obtain the CGBD, we look back at Fig. 2. This figure shows a phase space α vs θ. Now we consider different initial conditions, but all of them starting at $\alpha_0 = \pi/2$ (green dotted horizontal line passing through $\alpha = \pi/2$), and the initial angle θ is chosen in the interval $\theta_0 \in [0, 2\pi]$. So, we are taking only a portion of the phase space, and studying what happens in such a figure. For example, observe Fig. 2, following the dotted horizontal line passing through $\alpha = \pi/2$, we see two huge periodic islands, where their centers are located at $\theta = \pi/2$ and $\theta = 3\pi/2$ (green crosses). Four other periodic islands (two purple and two yellow crosses) are also observed. So, as a conclusion, following line $\alpha = \pi/2$, one can observe how many islands there are. The CGBD is then used to check the presence of islands and also if they suffered duplications of period or disappeared (direct and inverse parabolic bifurcations) [22].

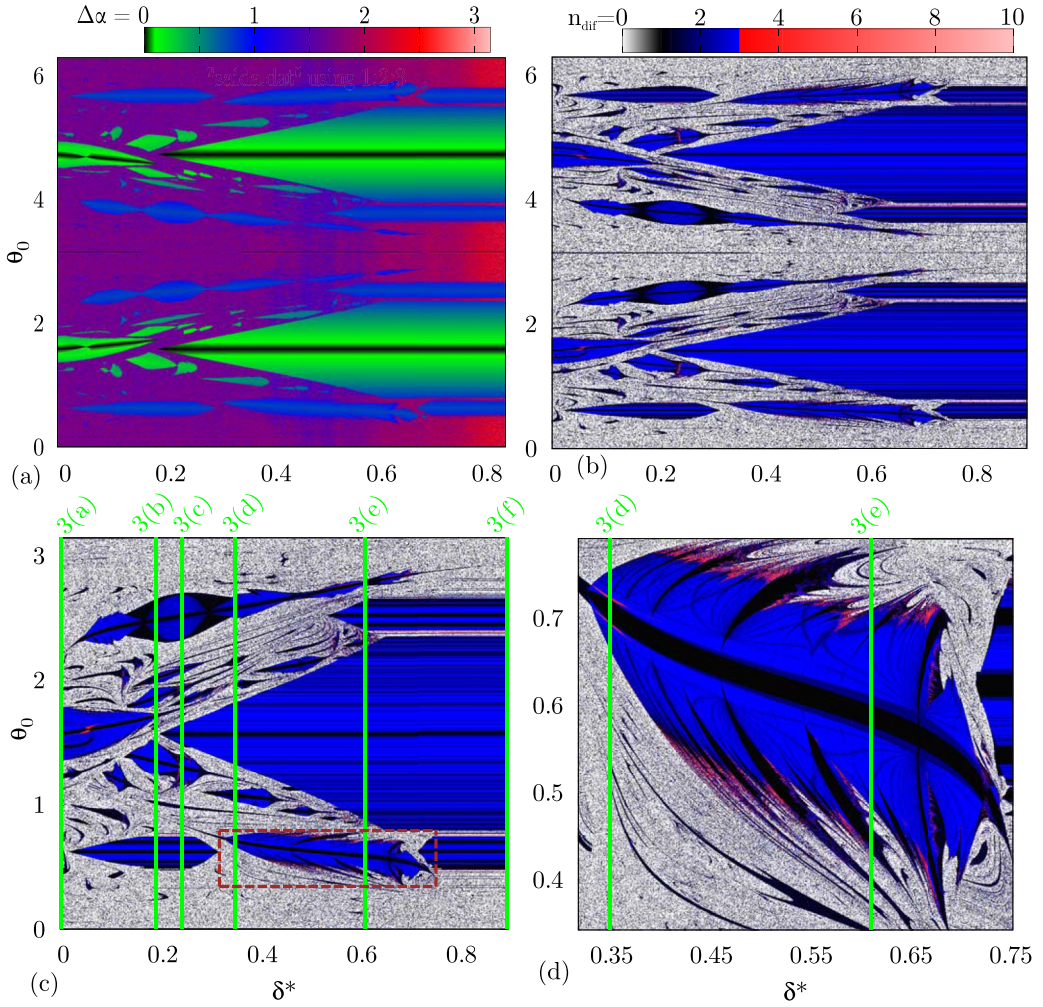

FIG. 4. Conservative generalized bifurcation diagrams θ_0 vs δ^*, where the colors represent in (a) the observable $\Delta\alpha$ [see Eq. (22)] and in (b)–(d) the number of different returning times n_{dif}. Panel (c) is a representation of the bottom half of item (b). Panel (d) is a magnification of the brown rectangle in (c). The control parameters used were $p = 2$, $\epsilon = 0.1$, $r^* = 0.2$, and $\eta = 1.1$.

Let us start by showing how to produce Fig. 4(a). Consider 1000×1000 equally spaced values of δ^* and $\theta_0 \in (0, 2\pi)$, with $\alpha_0 = \pi/2$ as previously mentioned. For each combination of δ^* and θ_0 an orbit is iterated up to 10^3 times. In this mean time, we calculate the maximum (α_{max}) and mininum (α_{min}) values of α found. So, the observable $\Delta\alpha$ was calculated using

$$\Delta\alpha = \alpha_{\text{max}} - \alpha_{\text{min}}. \tag{22}$$

It indirectly measures the spread, in the α axis, of the orbit in the phase space. If we have a periodic island, and its center is positioned in a horizontal line that passes through $\alpha = \pi/2$, it is going to be highlighted in Fig. 4(a) as the black regions, corresponding to a fixed point. If the color is green or blue, it means that the center of the island is not in $\alpha = \pi/2$, but is near that in a quasiperiodic curve. In summary, the colors black, green, and blue are highlighting periodic islands observed in $\alpha = \pi/2$. What we need to pay attention to is that we are changing the value of δ^* in the horizontal axis of Fig. 4(a). The other colors (purple and red) basically highlight chaotic regions. An important result is to observe what happens when $\delta^* \to \delta^*_{\text{max}}$, given by Eq. (21). As one can see, the chaos is red in such a region, meaning that $\Delta\alpha \to \pi$ when $\delta^* \to \delta_{\text{max}}$. In conclusion, observing Eq. (22), one can argue that $\alpha_{\text{max}} \to \pi$ and $\alpha_{\text{min}} \to 0$, which means that the chaotic sea destroyed all the invariant spanning curves, expanding its *size*, as shown and explained in Fig. 3(f).

The other observable used in this paper, in order to generate the CGBD, is the number of different returning times (n_{dif}), where the results are shown in Figs. 4(b)–4(d). To construct such figures, we choose 1000×1000 different values of δ^* and θ_0 for $\alpha_0 = \pi/2$. The main idea is to count the number of iterations until an orbit returns near the initial condition. It can be done by evaluating the following conditions:

$$|\theta_{n+1} - \theta_0| < 0.5\% \times 2\pi \text{ and } |\alpha_{n+1} - \alpha_0| < 0.5\% \times 2\pi. \tag{23}$$

The measure $0.5\% \times 2\pi$ is a portion of the maximum size of the phase space (which is 2π for θ), and the value 0.5% was chosen because apparently it could give us better results. If both conditions are true, then we save the number of iterations

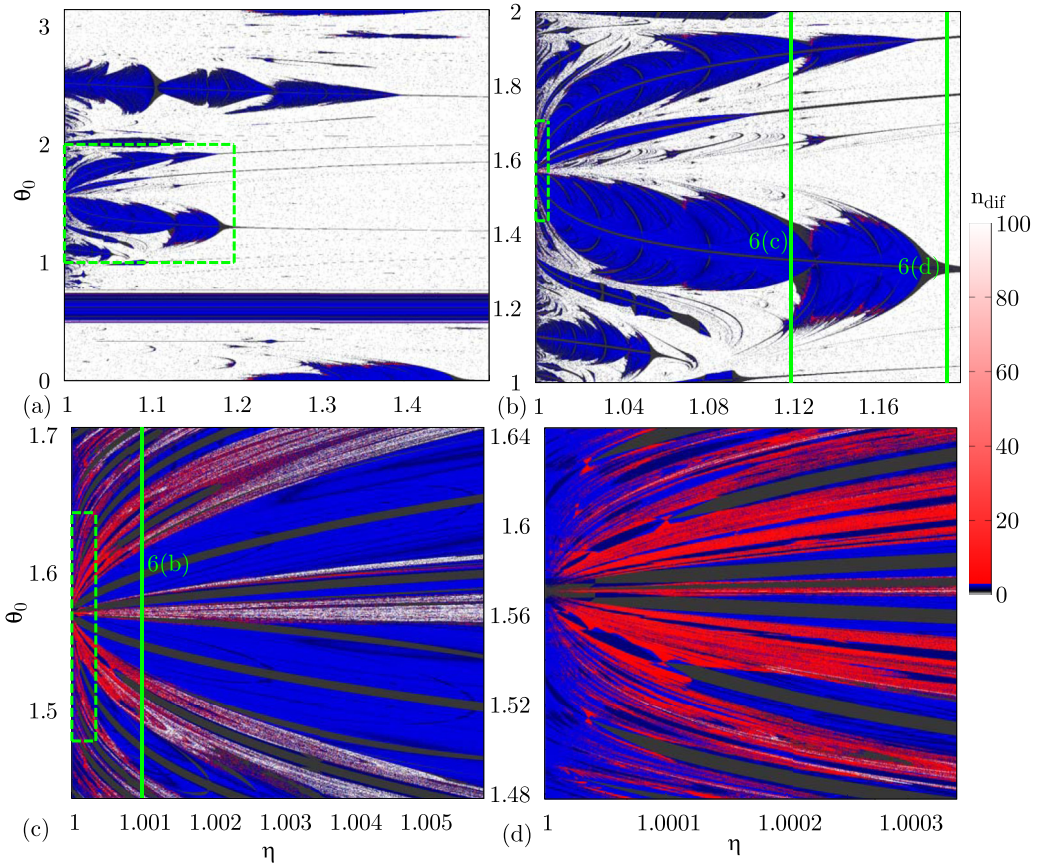

FIG. 5. Conservative generalized bifurcation diagrams θ_0 vs η, where the colors represent the number of different returning times n_{dif}. Panel (b) is a magnification of the rectangle in item (a), while panel (c) is a magnification of the rectangle in (b). Finally (d) is a magnification in the rectangle shown in (c). The control parameters used were $p = 2$, $\epsilon = 0.1$, and $r^* = \delta^* = 0.2$.

and start counting again the number of iterations. According to Slater's theorem [23], a quasiperiodic orbit on an irrational torus has at maximum three different returning times, while chaotic orbits have more than that.

In Fig. 4(b) we present the results, for which depending on the value of n_{dif} a different color was set. We chose a continuous color grid from 0 (white) to 1 (black), and after that it goes from 1 to 3 (blue). Higher values of n_{dif} were set from red to pink. $n_{\text{dif}} = 0$ (null returning time) means that the orbit does not return to the neighborhood of (θ_0, α_0). As one can see, this figure presents a clear symmetry in the vertical. So, amplifying the bottom half of this figure, one can see with more detail what is happening, and the result is shown in Fig. 4(c). In this figure, we marked, as green vertical lines, some interesting values of δ^*. For example, the first line shows a cut of the phase space (in $\alpha = \pi/2$) with $\delta^* = 0$, which was shown in Fig. 3(a). So, each vertical line is one of the items shown in Figs. 3(a)–3(f). The black regions in Fig. 4(c) are the center of periodic islands. The huge black to blue region in the right side of this figure is the big periodic island, which starts recovering its shape when we increase the value of δ^*. In the second line [with index 3(b)], the fixed point at $\theta = \pi/2$ disappears completely and the chaotic sea takes the place of this region confirming the previous result shown in Fig. 3(b), where we had seen that the fixed point had disappeared. The last line [named as 3(f)] shows the limit case ($\delta^* = \delta^*_{\text{max}}$), where there are no invariant spanning curves and the two huge periodic islands are observed [see Fig. 3(f)].

Figure 4(d) shows an enlargement in the brown rectangle of Fig. 4(c). This figure shows details about one of the periodic islands, where it disappears at $\delta^* \cong 0.75$. This figure has a fractal structure at the borders, shown with details in Refs. [21,22].

Now we start changing the amplitude of η, which indirectly changes the refraction index of n_1 and n_2. In Fig. 5(a) we show the CGBD for $\delta^* = 0.2$, $p = 2$, $\epsilon = 0.1$, and $r^* = 0.2$. As one can see in such figure, a complex behavior of the fixed points is observed. In particular, after an enlargement of the green rectangle, we obtain Fig. 5(b), which shows some details about the fixed points near $\theta = \pi/2$. Applying a new enlargement in the green rectangle, one can obtain Fig. 5(c). Such a figure shows with details that after introducing the tunable refraction index, one can raise a very intrinsic behavior of the fixed points, and a lot of them appear near $\theta = \pi/2$. Another enlargement is shown in Fig. 5(d).

Now we show how the variation of η, considered in Figs. 5(a)–5(d), affects the phase space of the system. To do so, first we plot Fig. 6(a), which considers $r^* = \delta^* = 0.2$, $\eta = 1$, $p = 2$, and $\epsilon = 0.1$. In such case, similar results to the mirrored version of the inner circle are reproduced. In such

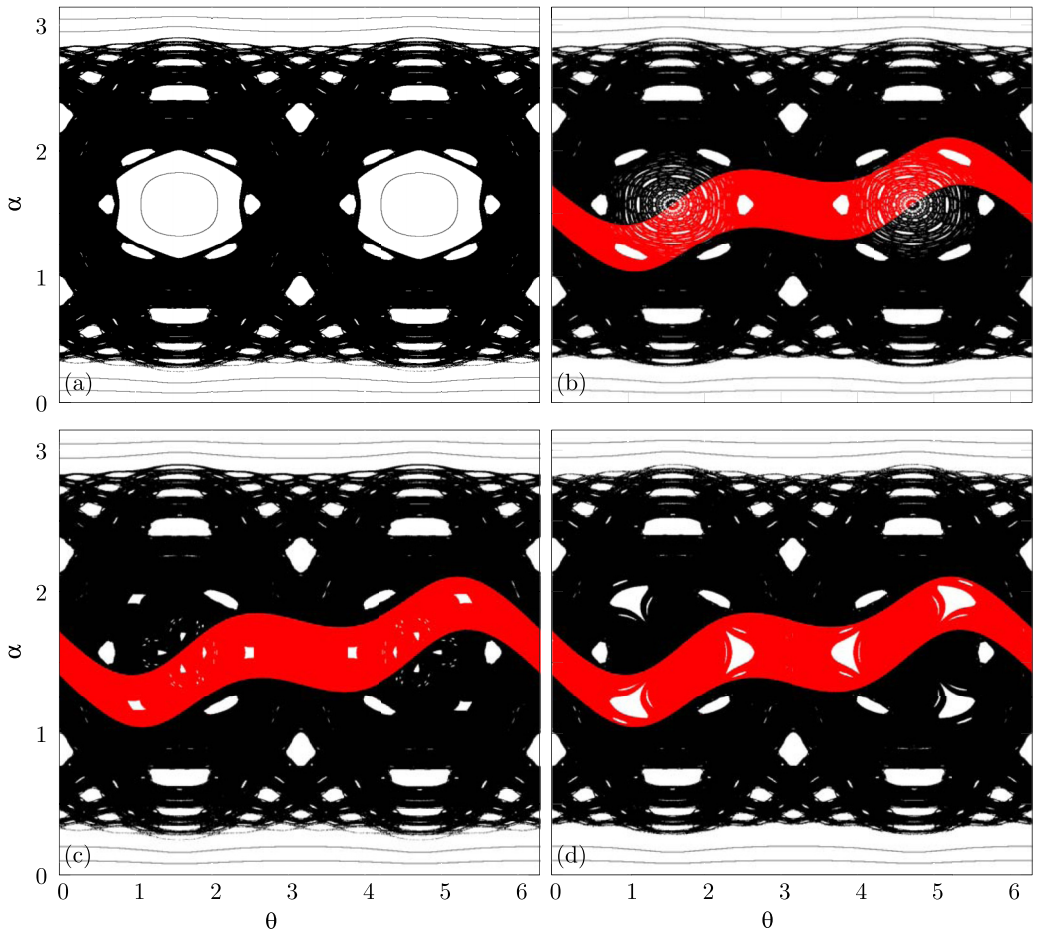

FIG. 6. Phase space θ vs α for $p = 2, \epsilon = 0.1, r^* = \delta^* = 0.2$ and for different values of η. Panel (a) shows the results for $\eta = 1$. In (b) the value of η was changed to 1.001, while in (c) the value of η is 1.12 and in (d) $\eta = 1.1936$.

case we see a chaotic sea for an orbit starting from $\theta_0 = 0.01$ and $\alpha_0 = \pi/2 - 0.01$. A big periodic island is observed in $(\theta, \alpha) = (\pi/4, \pi/2)$. Now you need to observe Fig. 5(c). In such figure, we highlighted a straight line with $\eta = 1.001$. Considering this combination of control parameters, we constructed Fig. 6(b). We observe that the periodic islands now are broken into several small periodic islands, and a chaotic orbit now can travel inside the region in which we have only periodic regions in Fig. 6(a). It explains what happens in Fig. 5(c), in which we have a proliferation of periodic orbits near $\theta = \pi/4$.

Figure 6(c) refers to a cut in Fig. 5(b), which highlights the results for $\eta = 1.12$. Here one can see that the number of islands is smaller than Fig. 6(b). Finally, we changed the control parameter to $\eta = 1.1936$ [which is another cut in the CGBD shown in Fig. 5(b)], and the results are shown in Fig. 6(d). Basically, when changing the value of η, for the combination of control parameters taken, we are changing the same portion of the phase space, but the results vary depending on the value of η.

V. FINAL REMARKS

In this work we present part of a study that is in development concerning properties of the optical oval billiard. We present the behavior of a light beam under the effect of a tunable-refractive index in the circular scatter. The inner side of the external boundary is considered a perfect reflector in such a way that a light beam suffers complete reflection, and when there is not the inner scatter, this means unitary refractive index, the corresponding phase space presents two huge stability regions. On the other hand, when the inner scatter is introduced, a sudden change occurs in previous stability regions and another region is characterized in the plots through red color. This is the region which corresponds to the light trajectories that refracts in the refractive scatter. That red region is very sensitive to the position of the center of the circular scatter. As the eccentricity (δ^*) increases, this region suffers deformations and expressively alters their neighborhood. In the limit case of maximum eccentricity it stretches vertically and destroys all whispering gallery orbits. It is worth pointing out that there are persistent small resonance structures along the red layer for any value of the eccentricity. The conservative generalized bifurcation diagram technique, and the returning times as well, are also presented to show the finest structures of the dynamics. As the eccentricity is changed we observe the transformation of the huge stable structures cited above and a very rich set of bifurcations. On the other hand, the increase of the refractive index changes the neighborhood of the central elliptic fixed point, so that the

center of stability in the phase space is destroyed, which leads to a dispersion of scattered light. In place of the huge stability islands appear pulverized islands, changing the structure of the traps for the light propagation. This suggests that the tunable refractive index allows one to vary the light coding transmission. Further studies with the optical oval billiard are in preparation.

ACKNOWLEDGMENTS

D.R.C. acknowledges PNPD/CAPES-Coordination for the Improvement of Higher Education Personnel. R.E.C. thanks CNPq–National Council for Scientific and Technological Development through Grant No. 306034/2015-8 and FAPESP–São Paulo Research Foundation through Grant No. 14/00334-9.

[1] K. Ikeda and O. Akimoto, Instability Leading to Periodic and Chaotic Self-Pulsations in a Bistable Optical Cavity, Phys. Rev. Lett. **48**, 617 (1982).

[2] F. T. Arecchi and R. Meucci, Chaos in optics, Scholarpedia **3**, 4104 (2008).

[3] D. Navarro-Urrios, N. E. Capuj, M. F. Colombano, P. D. García, M. Sledzinska, F. Alzina, A. Griol, A. Martínez, and C. M. Sotomayor-Torres, Nonlinear dynamics and chaos in an optomechanical beam, Nat. Commun. **8**, 14965 (2017).

[4] J.-P. Eckmann and I. Procaccia, *Spatio-Temporal Chaos*, (Springer US, Boston, 1991), pp. 135–172.

[5] M. C. Cross and P. C. Hohenberg, Spatiotemporal chaos, Science **263**, 1569 (1994).

[6] L. A. Bunimovich and Y. G. Sinai, Spacetime chaos in coupled map lattices, Nonlinearity **1**, 491 (1988).

[7] F. Selmi, S. Coulibaly, Z. Loghmari, I. Sagnes, G. Beaudoin, M. G. Clerc, and S. Barbay, Spatiotemporal Chaos Induces Extreme Events in an Extended Microcavity Laser, Phys. Rev. Lett. **116**, 013901 (2016).

[8] R. W. Boyd and A. L. Gaeta, Chaos in Nonlinear Optics, in *Laser Optics of Condensed Matter* (Springer, New York, 1991), pp. 99–105.

[9] F. T. Arecchi, S. Boccaletti, and P. Ramazza, Pattern formation and competition in nonlinear optics, Phys. Rep. **318**, 1 (1999).

[10] L. Lugiato, Transverse nonlinear optics: Introduction and review, Chaos Solitons Fractals **4**, 1251 (1994).

[11] P. W. Milonni, J. R. Ackerhalt, and H. W. Galbraith, Chaos and nonlinear optics: A chaotic raman attractor, Phys. Rev. A **28**, 887 (1983).

[12] L. Illing, D. J. Gauthier, and R. Roy, Controlling optical chaos, spatio-temporal dynamics, and patterns, Adv. At., Mol., Opt. Phys. **54**, 615 (2007).

[13] A. Argyris, D. Syvridis, L. Larger, V. Annovazzi-Lodi, P. Colet, I. Fischer, J. Garcia-Ojalvo, C. R. Mirasso, L. Pesquera, and K. A. Shore, Chaos-based communications at high bit rates using commercial fibre-optic links, Nature (London) **438**, 343 (2005).

[14] J. M. V. Grzybowski, M. Eisencraft, and E. E. N. Macau, Chaos-based communication systems: Current trends and challenges, *Applications of Chaos and Nonlinear Dynamics in Engineering* (Springer, New York, 2011), Vol. 1, pp. 203–230.

[15] S. Hayes, C. Grebogi, and E. Ott, Communicating with Chaos, Phys. Rev. Lett. **70**, 3031 (1993).

[16] S. Hayes, C. Grebogi, E. Ott, and A. Mark, Experimental Control of Chaos for Communication, Phys. Rev. Lett. **73**, 1781 (1994).

[17] D. V. Strekalov, C. Marquardt, A. B. Matsko, H. G. Schwefel, and G. Leuchs, Nonlinear and quantum optics with whispering gallery resonators, J. Opt. **18**, 123002 (2016).

[18] D. David, D. D. Holm, and M. Tratnik, Hamiltonian chaos in nonlinear optical polarization dynamics, Phys. Rep. **187**, 281 (1990).

[19] O. Bohigas, D. Boosé, R. E. de Carvalho, and V. Marvulle, Quantum tunneling and chaotic dynamics, Nucl. Phys. A **560**, 197 (1993).

[20] R. Egydio de Carvalho, Overlap of isochrone resonances: Chaos and refraction, Phys. Rev. E **55**, 3781 (1997).

[21] D. R. da Costa, C. P. Dettmann, J. A. de Oliveira, and E. D. Leonel, Dynamics of classical particles in oval or elliptic billiards with a dispersing mechanism, Chaos **25**, 033109 (2015).

[22] C. Manchein and M. W. Beims, Conservative generalized bifurcation diagrams, Phys. Lett. A **377**, 789 (2013).

[23] N. B. Slater, Gaps and steps for the sequence $n\theta$ mod 1, Math. Proc. Cambridge Philos. Soc. **63**, 1115 (1967).